Mixed-Ligand Driven Phase-Pure 2D Perovskite for Interfacial Passivation of Perovskite Photovoltaics

Meng-Chen Shih,[1] Shaun Tan,[1] Yongli Lu,[1] Tim Kodalle,[2,3] Tanguy Terlier,[4,5] Matthias J. Grotevent,[1] Faiz Mandani,[5] Ruiqi Zhang,[6] Do-Kyoung Lee,[2,7] Yu-Kuan Lin,[1,8] Hua Zhu,[1] Carolin M. Sutter-Fella,[2] Aditya Mohite,[5] Vladimir Bulović,[6] Moungi G. Bawendi[1]*

[1]Department of Chemistry, Massachusetts Institute of Technology, 77 Massachusetts Avenue, Cambridge, Massachusetts 02139, USA

[2]Molecular Foundry Division, Lawrence Berkeley National Laboratory, 67 Cyclotron Road, Berkeley, California 94720, USA

[3]Advanced Light Source, Lawrence Berkeley National Laboratory, 6 Cyclotron Road, Berkeley, California 94720, USA

[4]SIMS laboratory, Shared Equipment Authority, Rice University, 6100 Main Street, 77005 Houston Texas, United States.

[5]Department of Chemical & Biomolecular Engineering, Rice University, Houston, TX 77005, USA.

[6]Department of Electrical Engineering and Computer Science, Massachusetts Institute of Technology (MIT), 77 Massachusetts Avenue, Cambridge, Massachusetts 02139, USA

[7]Nevada Extreme Conditions Laboratory, University of Nevada, Las Vegas, Nevada 89154, United States

[8]Department of Materials Science and Engineering, Massachusetts Institute of Technology, 77 Massachusetts Avenue, Cambridge, Massachusetts 02139, USA

ABSTRACT: Effective interfacial passivation is essential for achieving high-performance perovskite photovoltaics. 2D/3D heterostructures are a widely adopted strategy for defect passivation and band alignment regulation. Despite recent progress, achieving favorable interfacial energetics and comprehensively suppressing nonradiative recombination at both surfaces and grain boundaries continues to be an active area of investigation. We introduce a co-assembled 2D architecture in which long-chain ligands are complemented by a minority component of short-chain ligands to form a mixed-ligand passivation layer. Such a co-assembled structure promotes preferentially phase-pure, n = 2, 2D layer formation, resulting in an energetically favorable band alignment that enhances charge extraction. In addition, this co-assembly facilitates effective passivation of interfacial defects at both surfaces and grain boundaries, leading to suppressed nonradiative recombination. As a consequence, these interfacial improvements increase carrier lifetimes and enhance the fill factor and open-circuit voltage of the device, yielding a higher power-conversion efficiency.

INTRODUCTION

Metal halide perovskite solar cells (PSCs) have emerged as one of the most promising next-generation photovoltaic technologies, offering outstanding power-conversion efficiencies (PCEs), tunable optoelectronic properties, and low-temperature solution processability.[1-4] In recent years, interfacial passivation, particularly via 2D/3D heterostructures (where, in this work, the term "2D" is used as a unified designation for layer perovskites, including both 2D and quasi-2D perovskite), has become a widely adopted approach to further enhance device performance, given their capability to suppress surface defects, block ion migration, and tune interfacial energetics.[5-10] However, in the conventional long-chain 2D treatments, the resulting 2D layers often contain impure 2D phases due to rapid and uncontrolled nucleation.[11,12] Such phase disorder induces unfavorable band alignment at the perovskite interface, impeding charge extraction and transport.[13] Furthermore, with conventional long-chain 2D treatments, surface defects are preferentially passivated while grain-boundary defects remain largely untreated.[14] These unpassivated grain boundaries act as nonradiative recombination centers and ion migration pathways, accelerating charge losses and long-term degradation.[15,16]

Several molecular approaches have been reported as passivation for grain boundaries, including the use of cross-linkable monomers,[17] phosphonate diacid,[18] ammonium formate,[19] along with other molecular passivation agents.[20-22] Meanwhile, efforts to modulate band alignment have also been reported through solvent engineering,[7,23] organic ligand modification,[24,25] and process engineering.[26,27] Although these strategies have enabled notable improvements, they typically address either band alignment or grain-boundary passivation, rather than integrating both effects simultaneously. Consequently, achieving phase-pure 2D layers

with favorable band alignment while concurrently passivating grain boundaries remains an ongoing challenge.

We propose a co-assembled mixed-ligand strategy to construct a high-quality 2D interfacial layer. This approach is distinct from previous studies that have typically employed 1:1 mixed-ligand formulations, a stoichiometry that often suffers from intrinsic limitations such as structurally impure 2D phase formation or electronically unfavorable interfacial energetics, both of which limit efficient carrier extraction and do not necessarily lead to an improved device PCE relative to conventional long-chain 2D treatments.[28,29] We find that introducing only a minor amount of short-chain 2D additives into a long-chain ligand solution is sufficient to promote the preferential growth of phase-pure, n = 2, 2D layers. The resulting 2D layer provides an energetically favorable band alignment that facilitates more efficient charge extraction. Moreover, the short-chain additives promote deeper penetration of the long-chain ligands, leading to effective interfacial passivation of defects at both grain boundaries and the surface. As a result, the nip devices incorporating this treatment demonstrated notable enhancements in PCE, with the champion device reaching 25.7%.

RESULTS AND DISCUSSION

Challenges in Conventional Long-Chain 2D Treatments. In conventional long-chain 2D treatments, layered Ruddlesden–Popper (RP) 2D perovskites are formed on the 3D perovskite surface, following the general composition $L_2A_{n-1}Pb_nX_{3n+1}$. In this RP structure, L is a bulky organic spacer cation (e.g., octylammonium (OA^+) or hexylammonium (HA^+)) that separates the PbX_6 octahedral slabs, while the A-site cation (e.g., methylammonium (MA^+), formamidinium (FA^+), or Cs^+) and halide anions X^- reside within the inorganic octahedral framework. Each value of n corresponds to a specific 2D phase with distinct structural and electronic characteristics.[30,31] In practice, such RP-type 2D layers are commonly generated on the surface of a pre-formed 3D perovskite by applying a single ammonium ligand, which reacts with surface species to form a thin 2D overlayer that passivates surface defects, as illustrated in **Figure 1a**.[32,33] Compared to bare 3D devices, conventional long-chain 2D-treated devices exhibit improved device performance, as shown in **Figure S1**.

However, despite widespread use, two inherent challenges emerge from conventional long-chain 2D treatments. First, forming a phase-pure 2D layer is intrinsically difficult under conventional conditions. As shown in the in-situ grazing incident wide-angle X-ray scattering (GIWAXS) graph in **Figure 1b**, the growth of 2D perovskite typically follows a sequential pathway in which the n = 1, intermediate 2D phase, appears first and only partially converts into n=2, 2D phase, yielding an impure 2D phase. The resulting impure 2D interlayer, as shown in **Figure 1c**, leads to unfavorable interfacial energy levels hindering efficient carrier extraction.[34] Second, the organic ligands introduced in this treatment primarily accumulate at the perovskite surface, with minimal penetration into the bulk.[14] As a result, only surface traps are effectively suppressed, while defects in grain boundaries receive only limited passivation.

To address these challenges, we introduce a mixed-ligand 2D treatment in which long-chain ligands are supplemented with short-chain additives. In this mixed-ligand system, the short-chain additives modulate the interfacial assembly, enabling the long-chain ligands to form a preferentially phase-pure n = 2 2D layer. In addition, the short-chain components facilitate deeper penetration of the long-chain ligands into the grain-boundary, extending effective passivation from the surface into the bulk 3D perovskite.

Preferential Formation of Phase-Pure 2D layers. The mixed-ligand treatment process is schematically illustrated in **Figure 1a.** The evolution of the 2D phase under mixed-ligand treatment (a mixture of long-chain OA^+ and minor short-chain butylammonium (BA^+)) was probed by in-situ GIWAXS, as shown in **Figure 1d**. After annealing, the mixed-ligand treatment resulted in the rapid crystallization of a dominant n = 2 phase, while the n = 1 phase was barely detectable. This phase evolution ultimately leads to the formation of a phase-pure n = 2 structure, as evidenced by the ex-situ GIWAXS detector image shown in **Figure 1e**. To further compare the time-dependent 2D phase profile, we overlaid the time-dependent 2D patterns obtained from the mixed-ligand treatment with those from the conventional long-chain 2D treatment (**Figure 2a**). Unlike the sequential n = 1 → n = 2 transition observed for the conventional process, the mixed-ligand system shows an immediate dominance of the n = 2 phase. These results demonstrate that the mixed-ligand conditions promote the preferential growth of the n = 2 phase while simultaneously suppressing the formation of the n = 1 phase. Such preferential formation of 2D phases is beneficial for 2D phase stability, as a preferentially stabilized 2D phase reduces deleterious phase evolution.[7]

We further examined the role of different ligands in the formation of 2D phases using X-ray diffraction (XRD) and GIWAXS analyses. First, XRD and GIWAXS consistently show that mixed-ligand films exhibit diffraction features associated with the long-chain spacer and differ markedly from the short-chain-only control films (**Figures S2, S3**, and **1e**). These observations indicate that the resulting 2D architecture is dominated by the long-chain spacer. Next, we examined the contribution of the short-chain ligand to mixed-ligand 2D formation by analyzing concentration-dependent XRD patterns. As shown in **Figure S4a**, increasing the short-chain fraction leads to a systematic shift of the n = 2 diffraction peak to higher 2θ, accompanied by an increase in the integrated peak area, reflecting a progressive decrease in layer spacing and enhanced incorporation of the short-chain ligand into the 2D lattice. Notably, as shown in **Figure S4b**, a short-chain fraction as low as 1/8 is sufficient to yield a phase-pure n = 2 structure, with phase purity maintained for short-chain fractions between 1/8 and 1/4. In contrast, further increasing the short-chain content (≥ 1/2) leads to the appearance of additional 2D diffraction peaks. Overall, these results show that the short-chain ligand is incorporated into the 2D structure and promotes phase-pure, n = 2, 2D formation at optimized incorporation levels, while the long-chain spacer remains the dominant structural component.

To examine the generality of the mixed-ligand strategy, the long-chain spacer OA^+ was paired with a range of short-chain ligands, including MA^+, ethylammonium (EA^+), propylammonium (PA^+), and BA^+. In all cases, the mixed-ligand treatments consistently yield phase-pure, n = 2, 2D phases, as evidenced by the corresponding XRD (**Figure 2b**). Moreover, this strategy is not limited to a specific halide composition. When a short-chain iodide ligand (BAI) or chloride ligand (PACl) was introduced into the OA-based system, a similarly phase-pure 2D phase was obtained, as shown in **Figure S5**. By comparison, substituting the short-chain additive with a longer spacer (HA^+) results in impure 2D phase formation (**Figure S6**). Together, these results indicate that supplementing long-chain ligands with appropriate short-

chain additives robustly suppresses the formation of undesired phases, enabling phase-pure 2D formation across a broad range of ligand and halide compositions. This effect can be ascribed to the balance of van der Waals interactions between stacked organic spacer layers. Long-chain spacer cations tend to favor the formation of n = 1 2D phases due to stronger van der Waals interactions arising from enhanced packing between extended alkyl chains, whereas the incorporation of short-chain ligands reduces the overall van der Waals interaction strength, thereby disfavoring n = 1 phase formation.[35] As a result, a mixed-ligand system incorporating a minor fraction of a short-chain ligand promotes the formation of a phase-pure, n = 2, 2D structure.

Interfacial Passivation and Characterization. Time-of-flight secondary ion mass spectrometry (ToF-SIMS) depth profiling was employed to examine the spatial ion distribution in conventionally treated and mixed-ligand-treated films. Hereafter, the mixed-ligand-treated films and devices are referred to as 'target', while the conventionally treated counterparts are referred to as 'control'. As shown in **Figure 3a**, in the control sample, the long-chain cations (OA^+) are primarily confined to the near-surface region, with their signal intensity rapidly decaying into the bulk 3D perovskite. The target film, however, exhibits a markedly different depth distribution of the 2D ligand cations, as shown in **Figure 3b**. When co-introduced with BA^+, the long-chain cations (OA^+) extend beyond the near-surface region, exhibiting significantly enhanced penetration into the bulk 3D perovskite. These observations suggest that the mixed-ligand environment promotes the incorporation of long-chain ligands into the bulk 3D perovskite, with localization at grain boundaries favored by their bulky nature. A plausible explanation for this behavior is that, when co-introduced with BA^+, the shorter-chain BA^+ molecules can more readily penetrate into grain boundaries, as commonly reported for short-chain spacer cations.[36] The incorporation of BA^+ at grain boundaries is expected to locally modify the chemical environment, rendering it less hydrophilic and more alkyl-rich.[37,38] Such a change in interfacial environment may lower the energetic barrier for the incorporation of long-chain OA^+ cations, facilitating their penetration into grain boundaries where they can cooperatively contribute to defect passivation.

The influence of short-chain ligand concentration on OA^+ penetration was examined by systematically varying the BABr amount. As illustrated in **Figure S7**, changing the BABr concentration over the investigated range (BABr/OABr = 1/8 to 1/2) does not lead to pronounced changes in the OA^+ penetration profile. However, it is noteworthy that the introduction of only a minor amount of BABr (BABr/OABr = 1/8) is sufficient to alter the depth distribution of OA^+ within the film significantly. This behavior indicates that the presence of a small fraction of short-chain ligands is sufficient to enable OA^+ penetration to the grain boundaries of the 3D perovskite film, which is expected to facilitate grain-boundary passivation along with the short-chain ligands. To further examine the relationship between ligand penetration and defect passivation, time-resolved photoluminescence (TRPL) measurements were conducted. As shown in **Figure 3c**, the target films exhibit a pronounced enhancement in carrier lifetime, increasing by approximately 65% from 5.4 μs for the control to 8.9 μs for the target. Such a substantial increase indicates more effective suppression of nonradiative recombination pathways associated with interfacial and grain-boundary defects. This improvement is consistent with enhanced grain-boundary passivation enabled by the altered depth distribution and penetration of long-chain ligands under mixed-ligand conditions, as revealed by the ToF-SIMS analysis.

Surface and cross-sectional scanning electron microscopy (SEM) were conducted to examine the surface morphology and structural characteristics of the films. As shown in **Figure S8**, the bare 3D film contains some excess PbI_2 crystallites on the surface, which serve as a precursor for subsequent 2D perovskite formation.[7] In contrast, the control and target films both exhibit comparable grain sizes and compact, nearly pinhole-free morphologies, indicative of good film quality, with no obvious morphological differences observed between the two samples. To further examine the layer structure, cross-sectional SEM measurements were performed using films prepared with an increased 2D ligand concentration, allowing the 2D overlayer to be more readily resolved (**Figure S9**). Both the control and target samples exhibit comparable 3D perovskite and 2D overlayer thicknesses, as well as well-defined interfaces throughout the device stack, with no apparent differences in the overall structural features. These observations suggest that the differences in ligand distribution and passivation behavior between the control and target samples cannot simply be attributed to observable morphological or structural differences.

Ultraviolet photoelectron spectroscopy (UPS) was used to probe the interfacial energetics between the 3D perovskite and the HTL, Spiro-MeOTAD. The corresponding energy-level diagram is shown in **Figure 3d** and is based on the UPS measurements in **Figure S10**. The energy levels of the 3D perovskite, control, and target were determined from our UPS measurements, whereas the energy level of the HTL (Spiro-MeOTAD) was assigned based on the literature.[39,40] In the control samples, a type I band alignment is observed at the 3D perovskite/HTL interface, which can be attributed to the coexistence of n = 1 and n = 2, impure 2D phases, at the interface. This type I band alignment gives rise to an interfacial valence-band offset that impedes hole transfer, leading to increased series resistance in the devices. In contrast, a type II band alignment is observed at the 3D perovskite/HTL interface in the target films, which can be attributed to the formation of

a phase-pure, n = 2, 2D interlayer. This favorable type II band alignment establishes an energetic cascade across the interface, facilitating efficient hole transfer from the 3D perovskite into the HTL and mitigating resistive losses in the devices.

Device performance and stability. The photovoltaic performance of devices fabricated with an FTO/SnO_2/3D/2D/Spiro-OMeTAD/Au architecture is presented in **Figure 4a–d** for both the control and target. The statistical distribution of PCE shown in **Figure 4a** reveals a consistent performance enhancement in the target devices. Specifically, the average PCE increases from 24.0% to 25.0%, and a champion device delivers a PCE of 25.7%, underscoring the effectiveness of the mixed-ligand approach in improving device performance. Devices with the mixed-ligand approach also show only minor hysteresis (**Figure S11**).

Analysis of the photovoltaic parameters (**Figure 4b-d**) indicates that the PCE improvement primarily arises from increases in the open-circuit voltage (V_{OC}) and fill factor (FF). In contrast, the short-circuit current density (J_{SC}) remains comparable between the two device sets, with J_{SC} matching the external quantum efficiency (EQE) measurement in **Figure S12**. The enhanced V_{OC} reflects suppressed nonradiative recombination enabled by effective grain-boundary passivation, in agreement with the prolonged carrier lifetimes observed in TRPL measurements. In parallel, the improved FF indicates mitigated interfacial resistive losses enabled by efficient charge transport across the perovskite/HTL interface, arising from the favorable type-II energy alignment established by the formation of a phase-pure, n = 2, 2D perovskite layer. Collectively, these improvements in V_{OC} and FF lead to a notable enhancement in device PCE. The target devices also demonstrate sustained device performance during extended maximum power point (MPP) tracking measurements (**Figure S13**).

Conclusions. In summary, we demonstrate that mixed-ligand chemistry fundamentally governs the crystallization kinetics of 2D phases and the spatial distribution of 2D ligands within perovskite films. By balancing van der Waals interactions between 2D ligands, the incorporation of short-chain ligands suppresses the formation of the n = 1 phase and enables the preferential formation of a phase-pure, n = 2, 2D interlayer, establishing a favorable band alignment at the 2D/3D heterointerface. In addition, this mixed-ligand chemistry modifies the interfacial environment to facilitate the penetration of long-chain 2D ligands into 3D bulk grain boundaries, enabling concurrent passivation of surface and bulk defects. As a result, these interfacial improvements collectively improved charge extraction and suppressed nonradiative recombination, yielding prolonged carrier lifetimes and enhanced V_{OC} and FF. Consequently, nip devices employing the mixed-ligand treatment exhibit a notable enhancement in PCE, with a champion device reaching 25.7%, while maintaining device performance during extended MPP tracking measurements. This work highlights mixed-ligand chemistry as an effective strategy for achieving compositionally and interfacially controlled 2D/3D perovskite heterostructures.

ASSOCIATED CONTENT

Supporting Information

The Supporting Information is available free of charge on the ACS Publications website.

Additional experimental details, XRD, GIWAXS, ToF-SIMS, SEM, UPS, EQE, and device data

AUTHOR INFORMATION

Corresponding Author

Moungi G. Bawendi --- Department of Chemistry, Massachusetts Institute of Technology, 77 Massachusetts Avenue, Cambridge, Massachusetts 02139, USA; Email: mgb@mit.edu

Notes

M.-C.S., S.T., and M.G.B. are inventors of a provisional patent related to the subject matter of this manuscript. The other authors declare that they have no competing interests.

ACKNOWLEDGMENT

M.-C.S. and M.J.G. were supported by Active Surfaces, Inc. M.-C.S., Y.L., and R.Z. were funded by the U.S. Department of Energy, Solar Energy Technologies Office, under award no. DE-EE0009512. S.T. and Y.-K.L. were funded by the U.S. Department of Energy, Solar Energy Technologies Office, under award no. DE-EE0010503. H.Z. was funded by the U.S. Department of Energy (DOE), Office of Science, Office of Basic Energy Sciences, Materials Sciences and Engineering Division, under award number DE-SC0021650. T.K. acknowledges support by the U.S. Department of Energy (DOE), Office of Science, Office of Basic Energy Sciences, Materials Sciences and Engineering Division under Contract No. DE-AC02-05-CH11231 (D2S2 program KCD2S2). Work at the Advanced Light Source (ALS) was done at beamline 12.3.2 with support by Nobumichi Tamura. The ALS is a DOE Office of Science User Facility under contract no. DE-AC02-05CH11231. Beamtime studies were carried out with support from the Molecular Foundry, a user facility supported by the Office of Science, Office of Basic Energy Sciences, of the U.S. Department of Energy under Contract No. DE-AC02-05CH11231, under user proposal numbers MFP-8131 and -8491. D.-K.L. acknowledges the support of Chemical Sciences, Geosciences and Biosciences Division, Office of Basic Energy Sciences, Office of Science, U.S. Department of Energy under DOE Grant no. DE-SC-0023355. ToF-SIMS analyses were carried out with support provided by the National Science Foundation CBET-1626418. This work was conducted in part using resources of the Shared Equipment Authority at Rice University.

REFERENCES

(1) Green, M. A.; Dunlop, E. D.; Yoshita, M.; Kopidakis, N.; Bothe, K.; Siefer, G.; Hao, X.; Jiang, J. Y. Solar Cell Efficiency Tables (version 65). *Prog. Photovolt.* **2025**, *33* (1), 3–15.

(2) Chen, H.; Liu, C.; Xu, J.; Maxwell, A.; Zhou, W.; Yang, Y.; Zhou, Q.; Bati, A. S. R.; Wan, H.; Wang, Z.; Zeng, L.; Wang, J.; Serles, P.; Liu, Y.; Teale, S.; Liu, Y.; Saidaminov, M. I.; Li, M.; Rolston, N.; Hoogland, S.; Filleter, T.; Kanatzidis, M. G.; Chen, B.; Ning, Z.; Sargent, E. H. Improved Charge Extraction in Inverted Perovskite Solar Cells with Dual-Site-Binding Ligands. *Science* **2024**, *384* (6692), 189–193.

(3) Zhao, Y.; Ma, F.; Qu, Z.; Yu, S.; Shen, T.; Deng, H.-X.; Chu, X.; Peng, X.; Yuan, Y.; Zhang, X.; You, J. Inactive $(PbI_2)_2RbCl$ Stabilizes Perovskite Films for Efficient Solar Cells. *Science* **2022**, *377* (6605), 531–534.

(4) Zhou, J.; Luo, Y.; Li, R.; Tian, L.; Zhao, K.; Shen, J.; Jin, D.; Peng, Z.; Yao, L.; Zhang, L.; Liu, Q.; Zhang, S.; Jin, L.; Chu, S.; Wang, S.; Tian, Y.; Xu, J.; Zhang, X.; Shi, P.; Wang, X.; Fan, W.; Sun, X.; Sun, J.; Chen, L.-Z.; Wu, G.; Shi, W.; Wang, H.-F.; Deng, T.; Wang, R.; Yang, D.; Xue, J. Molecular Contacts with an Orthogonal π-Skeleton Induce Amorphization to Enhance Perovskite Solar Cell Performance. *Nat. Chem.* **2025**, *17* (4), 564–570.

(5) Sidhik, S.; Wang, Y.; Siena, M. D.; Asadpour, R.; Torma, A. J.; Terlier, T.; Ho, K.; Li, W.; Puthirath, A. B.; Shuai, X.; Agrawal, A.; Traore, B.; Jones, M.; Giridharagopal, R.; Ajayan, P. M.; Strzalka, J.; Ginger, D. S.; Katan, C.; Alam, M. A.; Even, J.; Kanatzidis, M. G.; Mohite, A. D. Deterministic Fabrication of 3D/2D Perovskite Bilayer Stacks for Durable and Efficient Solar Cells. *Science* **2022**, *377* (6613), 1425–1430.

(6) Jang, Y.-W.; Lee, S.; Yeom, K. M.; Jeong, K.; Choi, K.; Choi, M.; Noh, J. H. Intact 2D/3D Halide Junction Perovskite Solar Cells via Solid-Phase in-Plane Growth. *Nature Energy* **2021**, *6* (1), 63–71.

(7) Tan, S.; Shih, M.-C.; Lu, Y.; Choi, S.-G.; Dong, Y.; Lee, J.-H.; Yavuz, I.; Larson, B. W.; Park, S. Y.; Kodalle, T.; Zhang, R.; Grotevent, M. J.; Lin, Y.-K.; Zhu, H.; Bulović, V.; Sutter-Fella, C. M.; Park, N.-G.; Beard, M. C.; Lee, J.-W.; Zhu, K.; Bawendi, M. G. Spontaneous Formation of Robust Two-Dimensional Perovskite Phases. *Science* **2025**, *388* (6747), 639–645.

(8) Azmi, R.; Utomo, D. S.; Vishal, B.; Zhumagali, S.; Dally, P.; Risqi, A. M.; Prasetio, A.; Ugur, E.; Cao, F.; Imran, I. F.; Said, A. A.; Pininti, A. R.; Subbiah, A. S.; Aydin, E.; Xiao, C.; Seok, S. I.; De Wolf, S. Double-Side 2D/3D Heterojunctions for Inverted Perovskite Solar Cells. *Nature* **2024**, *628* (8006), 93–98.

(9) Wang, T.; Bi, L.; Yang, L.; Zeng, Z.; Ji, X.; Hu, Z.; Tsang, S.-W.; Yip, H.-L.; Fu, Q.; Jen, A. K.-Y.; Liu, Y. Dimensional Regulation from 1D/3D to 2D/3D of Perovskite Interfaces for Stable Inverted Perovskite Solar Cells. *J. Am. Chem. Soc.* **2024**, *146* (11), 7555–7564.

(10) Gao, Y.; Song, Z.; Fu, Q.; Chen, Y.; Yang, L.; Hu, Z.; Chen, Y.; Liu, Y. Controlled Nucleation and Oriented Crystallization of Methylammonium-Free Perovskites via in Situ Generated 2D Perovskite Phases. *Adv. Mater.* **2024**, *36* (33), e2405921.

(11) Zhao, X.; Liu, T.; Loo, Y.-L. Advancing 2D Perovskites for Efficient and Stable Solar Cells: Challenges and Opportunities. *Adv. Mater.* **2022**, *34* (3), e2105849.

(12) Azmi, R.; Ugur, E.; Seitkhan, A.; Aljamaan, F.; Subbiah, A. S.; Liu, J.; Harrison, G. T.; Nugraha, M. I.; Eswaran, M. K.; Babics, M.; Chen, Y.; Xu, F.; Allen, T. G.; ur Rehman, A.; Wang, C.-L.; Anthopoulos, T. D.; Schwingenschlögl, U.; Bastiani, M. D.; Aydin, E.; Wolf, S. D. Damp Heat–stable Perovskite Solar Cells with Tailored-Dimensionality 2D/3D Heterojunctions. *Science* **2022**, *376* (6588), 73–77.
(13) Proppe, A. H.; Quintero-Bermudez, R.; Tan, H.; Voznyy, O.; Kelley, S. O.; Sargent, E. H. Synthetic Control over Quantum Well Width Distribution and Carrier Migration in Low-Dimensional Perovskite Photovoltaics. *J. Am. Chem. Soc.* **2018**, *140* (8), 2890–2896.
(14) Zhou, L.; Lin, Z.; Ning, Z.; Li, T.; Guo, X.; Ma, J.; Su, J.; Zhang, C.; Zhang, J.; Liu, S.; Chang, J.; Hao, Y. Highly Efficient and Stable Planar Perovskite Solar Cells with Modulated Diffusion Passivation toward High Power Conversion Efficiency and Ultrahigh Fill Factor. *Sol. RRL* **2019**, *3* (11), 1900293.
(15) Zhou, W.; Chen, X.; Zhou, R.; Cai, H.; Wang, Y.; Zhang, T.; Zheng, Z.; Gao, F.; Zhang, Y.; Yan, H. The Role of Grain Boundaries on Ion Migration and Charge Recombination in Halide Perovskites. *Small* **2024**, *20* (32), e2310368.
(16) Tao, J.; Zhao, C.; Wang, Z.; Chen, Y.; Zang, L.; Yang, G.; Bai, Y.; Chu, J. Suppressing Non-Radiative Recombination for Efficient and Stable Perovskite Solar Cells. *Energy Environ. Sci.* **2025**, *18* (2), 509–544.
(17) Zhang, W.; Liu, J.; Song, W.; Shan, J.; Guan, H.; Zhou, J.; Meng, Y.; Tong, X.; Zhu, J.; Yang, M.; Ge, Z. Chemical Passivation and Grain-Boundary Manipulation via in Situ Cross-Linking Strategy for Scalable Flexible Perovskite Solar Cells. *Sci. Adv.* **2025**, *11* (5), eadr2290.
(18) Wang, K.; Xu, Z.; Guo, Z.; Wang, H.; Qaid, S. M. H.; Yang, K.; Zang, Z. Phosphonate Diacid Molecule Induced Crystallization Manipulation and Defect Passivation for High-performance Inverted MA-free Perovskite Solar Cells. *Adv. Energy Mater.* **2024**. *14*, 2402249.
(19) Ding, Y.; Wu, Y.; Feng, X.; Li, H.; Feng, E.; Chang, J.; Long, C.; Gao, Y.; Yang, J. Grain Boundary Cracks Patching and Defect Dual Passivation with Ammonium Formate for High-Efficiency Triple-Cation Perovskite Solar Cells. *Commun. Mater.* **2024**, *5* (1), 279.
(20) Kalluvila Justin, I. A.; Tiede, D. O.; Piot, M.; Forzatti, M.; Roldán-Carmona, C.; Galisteo-López, J. F.; Míguez, H.; Bolink, H. J. Strong Grain Boundary Passivation Effect of Coevaporated Dopants Enhances the Photoemission of Lead Halide Perovskites. *ACS Appl. Mater. Interfaces* **2024**, *16* (44), 61305–61313.
(21) Lu, Y.; Zhu, H.; Tan, S.; Zhang, R.; Shih, M.-C.; Grotevent, M. J.; Lin, Y.-K.; Choi, S.-G.; Lee, J.-W.; Bulović, V.; Bawendi, M. G. Stabilization of Organic Cations in Lead Halide Perovskite Solar Cells Using Phosphine Oxides Derivatives. *J. Am. Chem. Soc.* **2024**, *146* (32), 22387–22395.
(22) Li, Y.; Mo, H.; Wang, J.; Yuan, Z.; He, Y.; Zhu, T.; Fan, X.; Li, G.; Popović, J.; Djurišić, A. B. Grain Boundary Passivation as an Optimal Strategy for Perovskite Solar Cells with Improved Stability. *Sustain. Energy Fuels* **2025**, *9* (11), 3078–3087.
(23) Faheem, M. B.; Khan, B.; Zhang, Y.; Li, H.; Saud, M.; Lin, H.; Zhang, H.; Ahmed, S. B.; Vanshika, V.; Qiao, R.; Kaswekar, P.; Wang, Y.; Zheng, W.; He, J.-H.; Qiao, Q. Synergistic Solvent and Surface Engineering to Reduce V_{OC} Loss in Tin Halide Perovskite Solar Cells. *ACS Energy Lett.* **2025**, *10* (7), 3337–3348.
(24) Hu, J.; Oswald, I. W. H.; Stuard, S. J.; Nahid, M. M.; Zhou, N.; Williams, O. F.; Guo, Z.; Yan, L.; Hu, H.; Chen, Z.; Xiao, X.; Lin, Y.; Yang, Z.; Huang, J.; Moran, A. M.; Ade, H.; Neilson, J. R.; You, W. Synthetic Control over Orientational Degeneracy of Spacer Cations Enhances Solar Cell Efficiency in Two-Dimensional Perovskites. *Nat. Commun.* **2019**, *10* (1), 1276.
(25) Liu, P.; Li, X.; Cai, T.; Xing, W.; Yang, N.; Arandiyan, H.; Shao, Z.; Wang, S.; Liu, S. Molecular Structure Tailoring of Organic Spacers for High-Performance Ruddlesden-Popper Perovskite Solar Cells. *Nanomicro Lett.* **2024**, *17* (1), 35.
(26) Shih, M.-C.; Tan, S.; Lu, Y.; Kodalle, T.; Lee, D.-K.; Dong, Y.; Larson, B. W.; Park, S.; Zhang, R.; Grotevent, M. J.; Sverko, T.; Zhu, H.; Lin, Y.-K.; Sutter-Fella, C. M.; Zhu, K.; Beard, M. C.; Bulović, V.; Bawendi, M. G. A 2D/3D Heterostructure Perovskite Solar Cell with a Phase-Pure and Pristine 2D Layer. *Adv. Mater.* **2025**, *37* (17), e2416672.
(27) Kodalle, T.; Byranvand, M. M.; Goudreau, M.; Das, C.; Roy, R.; Kot, M.; Briesenick, S.; Zohdi, M.; Rai, M.; Tamura, N.; Flege, J. I.; Hempel, W.; Sutter-Fella, C. M.; Saliba, M. An Integrated Deposition and Passivation Strategy for Controlled Crystallization of 2D/3D Halide Perovskite Films. *Adv. Mater.* **2024**, *36* (24), e2309154.
(28) Mondal, S.; Eguchi, N.; Nishimura, N.; Hinuma, Y.; Yamamoto, K.; Kogo, A.; Murakami, T. N.; Kanda, H. Mixed 2D-Cation Passivation towards Improved Durability of Perovskite Solar Cells and Dynamics of 2D-Perovskites under Light Irradiation and at High Temperature. *Sustain. Energy Fuels* **2025**, *9* (1), 247–255.
(29) Abuhelaiqa, M.; Gao, X.-X.; Ding, Y.; Ding, B.; Yi, Z.; Sohail, M.; Kanda, H.; Dyson, P. J.; Nazeeruddin, M. K. Mixed Cation 2D Perovskite: A Novel Approach for Enhanced Perovskite Solar Cell Stability. *Sustainable Energy Fuels* **2022**, *6* (10), 2471–2477.
(30) Huo, C.; Cai, B.; Yuan, Z.; Ma, B.; Zeng, H. Two-dimensional Metal Halide Perovskites: Theory, Synthesis, and Optoelectronics. *Small Methods* **2017**, *1* (3), 1600018.
(31) Soe, C. M. M.; Nagabhushana, G. P.; Shivaramaiah, R.; Tsai, H.; Nie, W.; Blancon, J.-C.; Melkonyan, F.; Cao, D. H.; Traoré, B.; Pedesseau, L.; Kepenekian, M.; Katan, C.; Even, J.; Marks, T. J.; Navrotsky, A.; Mohite, A. D.; Stoumpos, C. C.; Kanatzidis, M. G. Structural and Thermodynamic Limits of Layer Thickness in 2D Halide Perovskites. *Proc. Natl. Acad. Sci. U. S. A.* **2019**, *116* (1), 58–66.
(32) Yoo, J. J.; Seo, G.; Chua, M. R.; Park, T. G.; Lu, Y.; Rotermund, F.; Kim, Y. K.; Moon, C. S.; Jeon, N. J.; Correa-Baena, J. P.; Bulović, V.; Shin, S. S.; Bawendi, M. G.; Seo, J. Efficient Perovskite Solar Cells via Improved Carrier Management. *Nature* **2021**, *590* (7847), 587–593.
(33) Chen, H.; Teale, S.; Chen, B.; Hou, Y.; Grater, L.; Zhu, T.; Bertens, K.; Park, S. M.; Atapattu, H. R.; Gao, Y.; Wei, M.; Johnston, A. K.; Zhou, Q.; Xu, K.; Yu, D.; Han, C.; Cui, T.; Jung, E. H.; Zhou, C.; Zhou, W.; Proppe, A. H.; Hoogland, S.; Laquai, F.; Filleter, T.; Graham, K. R.; Ning, Z.; Sargent, E. H. Quantum-Size-Tuned Heterostructures Enable Efficient and Stable Inverted Perovskite Solar Cells. *Nat. Photonics* **2022**, *16* (5), 352–358.
(34) Gu, H.; Xia, J.; Liang, C.; Chen, Y.; Huang, W.; Xing, G. Phase-Pure Two-Dimensional Layered Perovskite Thin Films. *Nature Reviews Materials* **2023**, *8*, 533–551.
(35) Xing, J.; Zhao, Y.; Askerka, M.; Quan, L. N.; Gong, X.; Zhao, W.; Zhao, J.; Tan, H.; Long, G.; Gao, L.; Yang, Z.; Voznyy, O.; Tang, J.; Lu, Z.-H.; Xiong, Q.; Sargent, E. H. Color-Stable Highly Luminescent Sky-Blue Perovskite Light-Emitting Diodes. *Nat. Commun.* **2018**, *9* (1), 1–8.
(36) Yang, G.; Ren, Z.; Liu, K.; Qin, M.; Deng, W.; Zhang, H.; Wang, H.; Liang, J.; Ye, F.; Liang, Q.; Yin, H.; Chen, Y.; Zhuang, Y.; Li, S.; Gao, B.; Wang, J.; Shi, T.; Wang, X.; Lu, X.; Wu, H.; Hou, J.; Lei, D.; So, S. K.; Yang, Y.; Fang, G.; Li, G. Stable and

Low-Photovoltage-Loss Perovskite Solar Cells by Multifunctional Passivation. *Nat. Photonics* **2021**, *15* (9), 681–689.
(37) Wygant, B. R.; Ye, A. Z.; Dolocan, A.; Vu, Q.; Abbot, D. M.; Mullins, C. B. Probing the Degradation Chemistry and Enhanced Stability of 2D Organolead Halide Perovskites. *J. Am. Chem. Soc.* **2019**, *141* (45), 18170–18181.
(38) Wu, W.-Q.; Yang, Z.; Rudd, P. N.; Shao, Y.; Dai, X.; Wei, H.; Zhao, J.; Fang, Y.; Wang, Q.; Liu, Y.; Deng, Y.; Xiao, X.; Feng, Y.; Huang, J. Bilateral Alkylamine for Suppressing Charge Recombination and Improving Stability in Blade-Coated Perovskite Solar Cells. *Sci. Adv.* **2019**, *5* (3), eaav8925.
(39) Euvrard, J.; Yan, Y.; Mitzi, D. B. Electrical Doping in Halide Perovskites. *Nat. Rev. Mater.* **2021**, *6* (6), 531–549.
(40) Peng, J.; Kremer, F.; Walter, D.; Wu, Y.; Ji, Y.; Xiang, J.; Liu, W.; Duong, T.; Shen, H.; Lu, T.; Brink, F.; Zhong, D.; Li, L.; Lee Cheong Lem, O.; Liu, Y.; Weber, K. J.; White, T. P.; Catchpole, K. R. Centimetre-Scale Perovskite Solar Cells with Fill Factors of More than 86 per Cent. *Nature* **2022**, *601* (7894), 573–578.

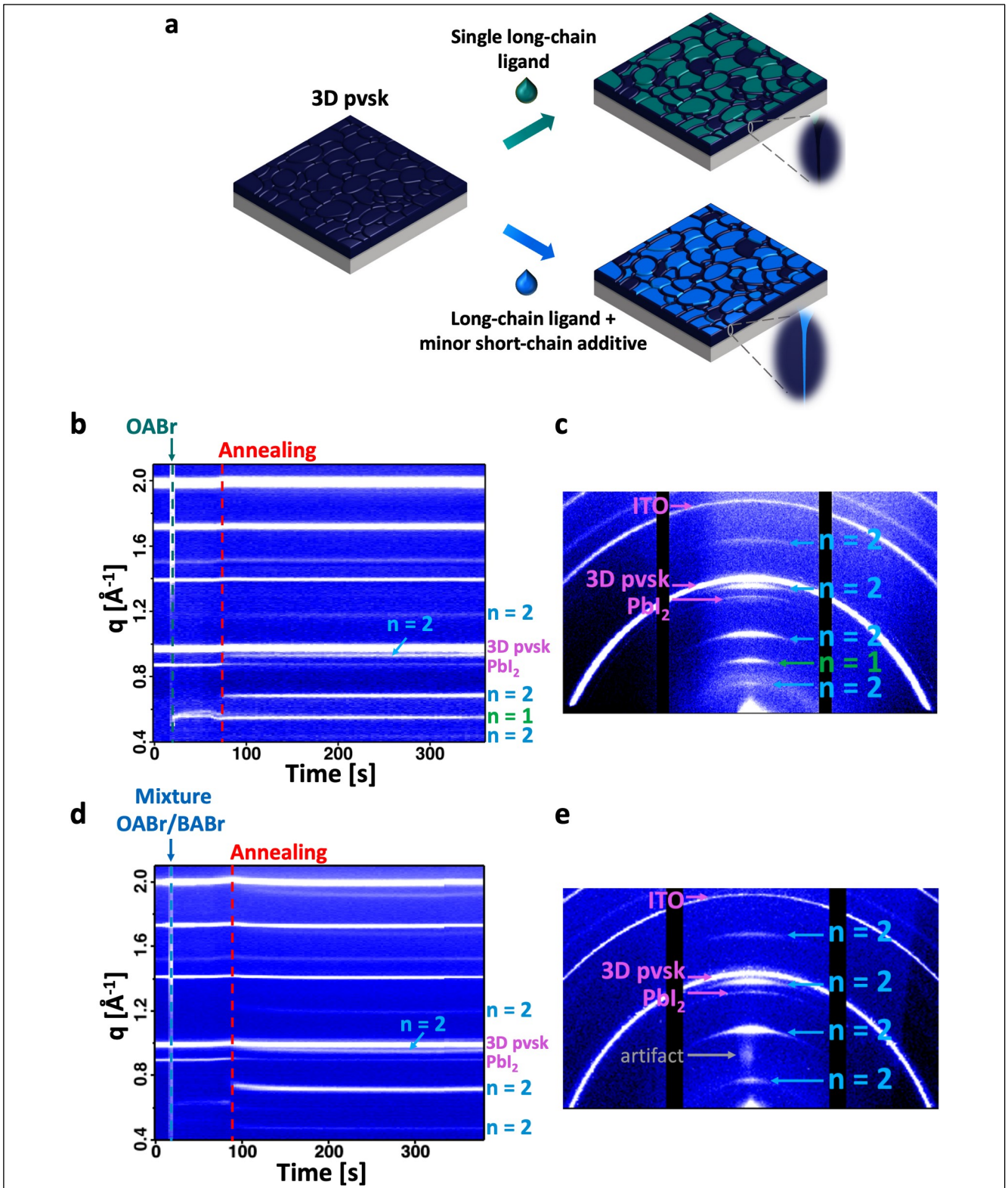

Figure 1. (a) Schematic illustration of the conventional long-chain 2D treatment and mixed-ligand treatment. (b,c) In-situ GIWAXS patterns and ex-situ GIWAXS detector image of films treated with the conventional long-chain 2D treatment (OABr). (d,e) In-situ GIWAXS patterns and ex-situ GIWAXS detector image of films treated with the mixed-ligand treatment (OABr/BABr).

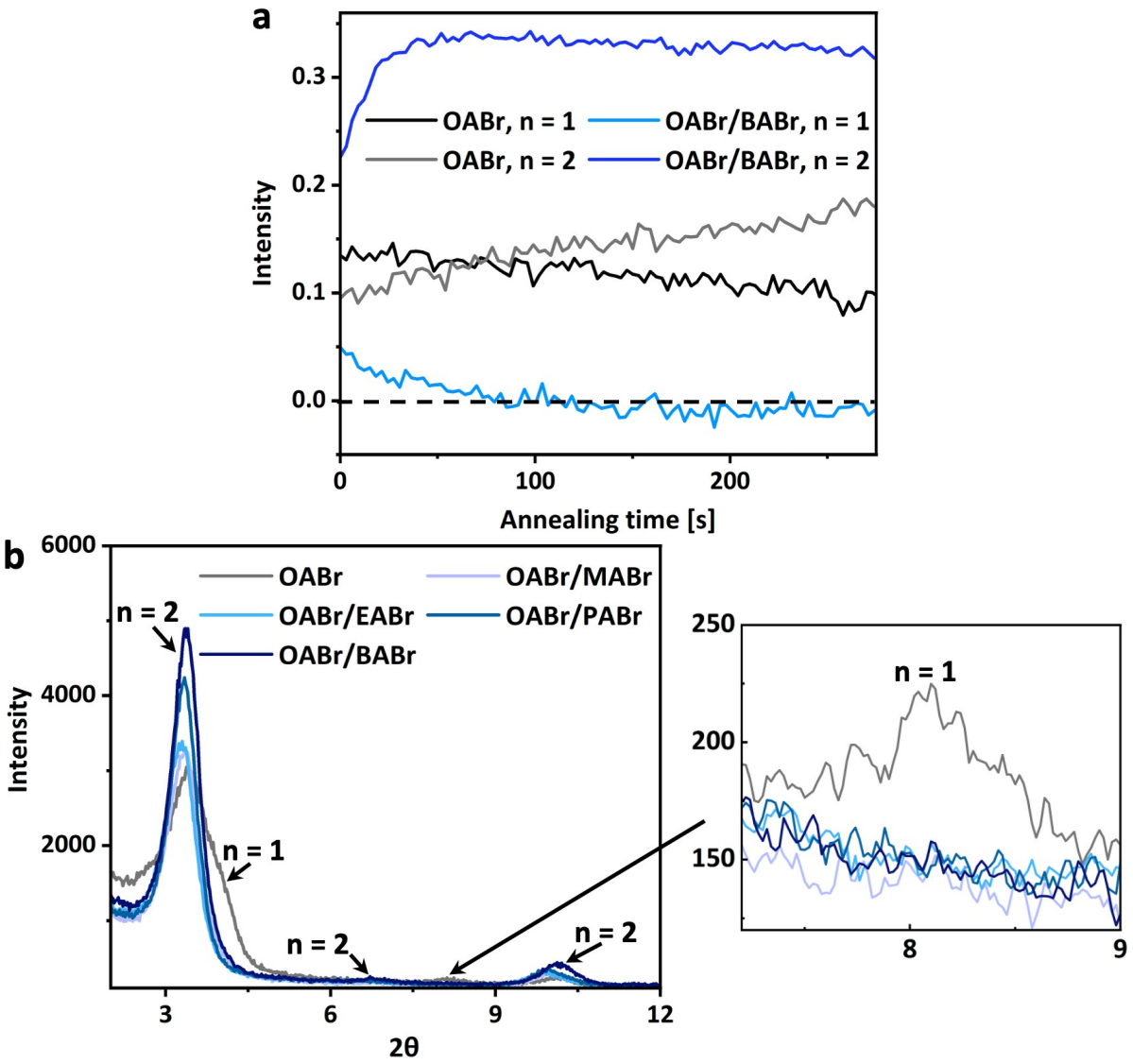

Figure 2. (a) Overlaid time-dependent integrated peak intensities of the n = 1 and n = 2 2D GIWAXS features extracted from the in-situ GIWAXS measurements of the conventional long-chain 2D treatment (**Figure 1b**) and mixed-ligand treatment (**Figure 1d**). (b) XRD patterns of films treated with mixed ligands comprising the long-chain spacer OA^+ and various short-chain ligand additives (MA^+, EA^+, PA^+, and BA^+).

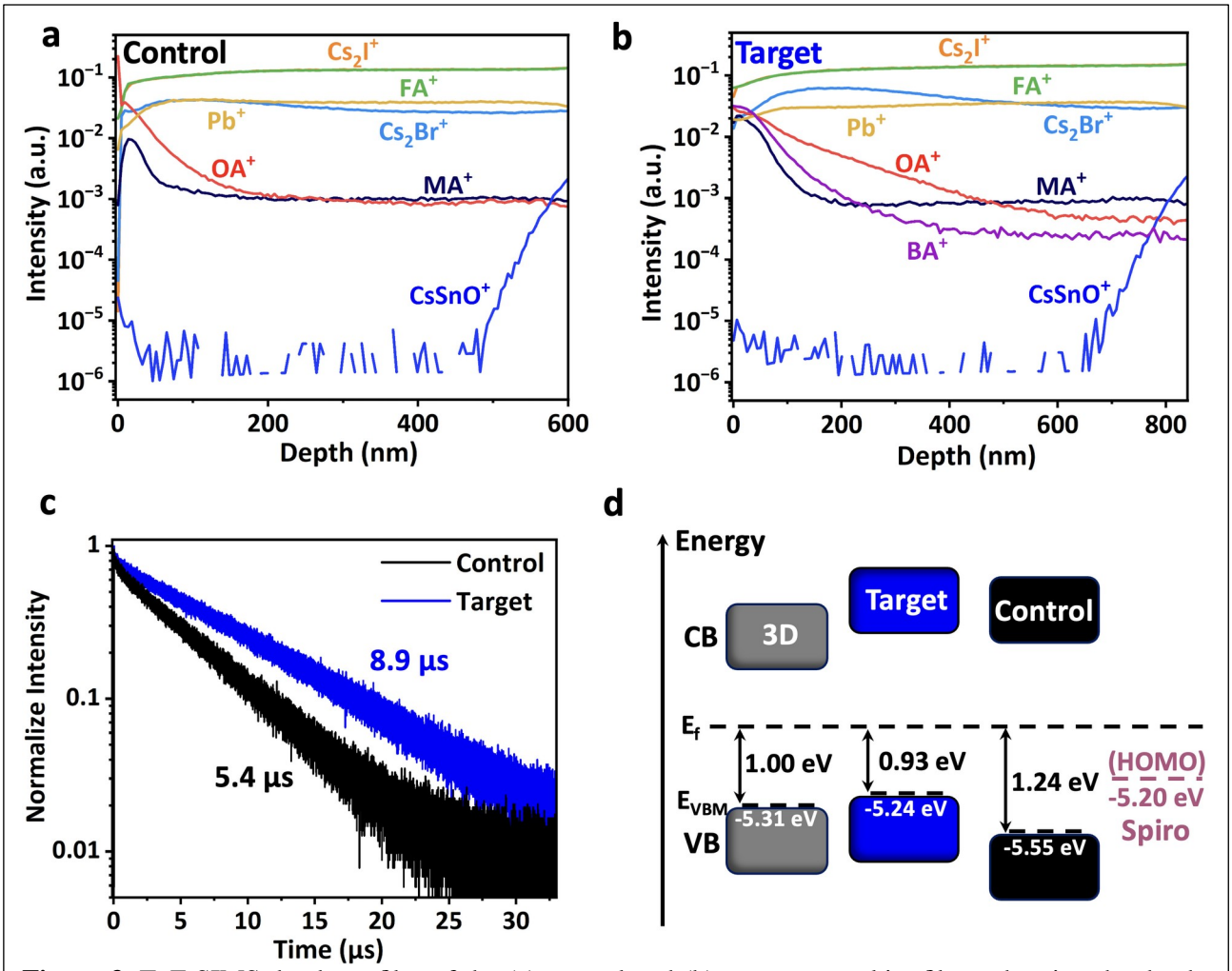

Figure 3. ToF-SIMS depth profiles of the (a) control and (b) target perovskite films, showing the depth-dependent distribution of selected ionic species. (c) TRPL spectra of the control and target perovskite films. (d) Schematic band diagram of the 3D perovskite and the 2D perovskite in the control and target films, with energy levels determined from UPS measurements (**Figure S10**), along with the HTL (Spiro-MeOTAD).

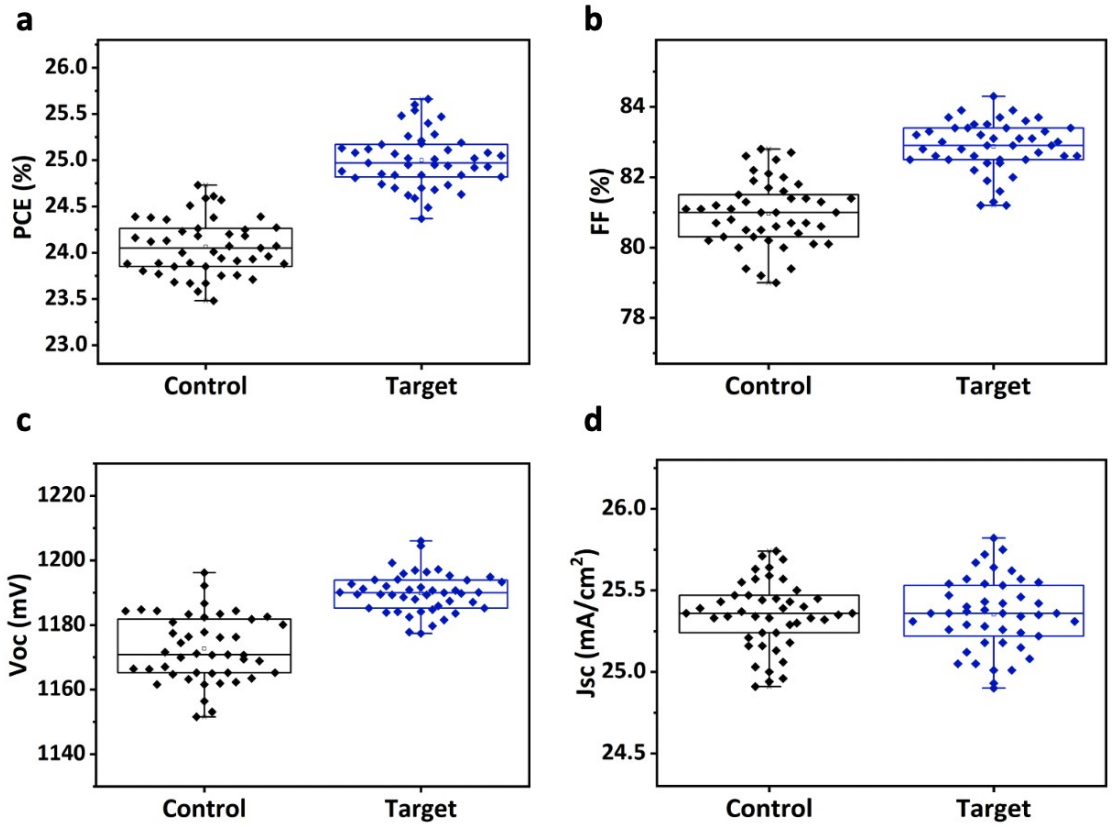

Figure 4. Statistics distributions of the (a) PCE, (b) *FF*, (c) *V*oc, and (d) *J*sc for the control and target devices.

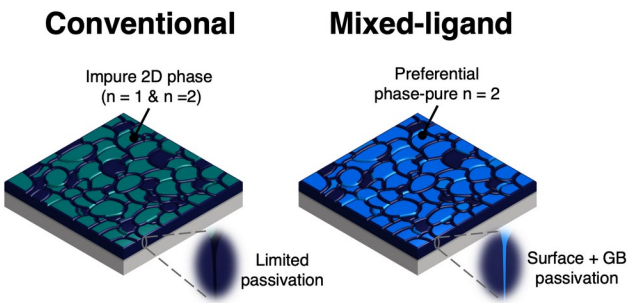
Conventional
Mixed-ligand
Impure 2D phase
(n = 1 & n =2)
Preferential
phase-pure n = 2
Limited
passivation
Surface + GB
passivation